Spatiotemporal ITCZ dynamics during the last three millennia in Northeastern Brazil and related impacts in modern human history

Giselle Utida[1]*, Francisco W. Cruz[1], Mathias Vuille[2], Angela Ampuero[1], Valdir F. Novello[3], Jelena Maksic[4], Gilvan Sampaio[5], Hai Cheng[6,7,8], Haiwei Zhang[6]; Fabio Ramos Dias de Andrade[1], R. Lawrence Edwards[9]

[1]Instittuto de Geociências, Universidade de São Paulo, Rua do Lago, 562, Cidade Universitária, São Paulo-SP, 05508-090, Brazil

[2]Department of Atmospheric and Environmental Sciences, University at Albany, SUNY, Albany, NY, USA

[3]Geo- and Environmental Research Center, University of Tübingen, Tübingen, Germany

[4]Division of Impacts, Adaptation and Vulnerabilities (DIIAV), National Institute for Space Research (INPE), São Jose dos Campos-SP, Brazil

[5]General Coordination of Earth Science (CGCT), National Institute for Space Research (INPE), São Jose dos Campos-SP, Brazil

[6]Institute of Global Environmental Change, Xi'an Jiaotong University, Xi'an, China

[7]State Key Laboratory of Loess and Quaternary Geology, Institute of Earth Environment, Chinese Academy of Sciences, Xi'an, China

[8]Key Laboratory of Karst Dynamics, MLR, Institute of Karst Geology, CAGS, China

[9]Department of Earth Sciences, University of Minnesota, Minneapolis, MN, USA

*Corresponding author: giselleutida@hotmail.com

28   *Abstract*

29   Changes in tropical precipitation over the past millennia have usually been associated with

30   latitudinal displacements of the Intertropical Convergence Zone (ITCZ). Recent studies

31   provide new evidence that contraction and expansion of the tropical rainbelt may also have

32   contributed to ITCZ variability on centennial time scales. Over tropical South America few

33   records point to a similar interpretation, which prevents a clear diagnosis of ITCZ changes

34   in the region. In order to improve our understanding of the equatorial rainbelt variability,

35   our study presents a reconstruction of precipitation for the last 3200 years from the

36   Northeast Brazil (NEB) region, an area solely influenced by ITCZ precipitation. We analyze

37   oxygen isotopes in speleothems that serve as a faithful proxy for the past location of the

38   southern margin of the ITCZ. Our results, in comparison with other ITCZ proxies, indicate

39   that the range of seasonal migration, contraction and expansion of the ITCZ was not

40   symmetrical around the equator on secular and multidecadal timescale. A new NEB ITCZ

41   pattern emerges based on the comparison between two distinct proxies that characterize

42   the ITCZ behavior during the last 2500 years, with an ITCZ zonal pattern between NEB

43   and the eastern Amazon. In NEB, the period related to the Medieval Climate Anomaly

44   (MCA – 950 to 1250 CE) was characterized by an abrupt transition from wet to dry

45   conditions. These drier conditions persisted until the onset of the period corresponding to

46   the Little Ice Age (LIA) in 1560 CE, representing the longest dry period over the last 3200

47   years in NEB. The ITCZ was apparently forced by teleconnections between Atlantic and

48   Pacific that controlled the position, intensity and extent of the Walker cell over South

49   America, changing the zonal ITCZ characteristics, while sea surface temperature changes

50   in both the Pacific and Atlantic, stretched/weakened the ITCZ-related rainfall meridionally

51   over NEB. Wetter conditions started around 1500 CE in NEB. During the last 500 years,

52   our speleothems document the occurrence of some of the strongest drought events over

53   the last centuries, which drastically affected population and environment of NEB during the

54   Portuguese colonial period. The historical droughts were able to affect the karst system,

55   and led to significant impacts over the entire NEB region.

56   *Keywords*: Holocene, stalagmites, stable isotopes, droughts, Portuguese colony

57

58   *1. Introduction*

59   Northeastern Brazil (NEB) is one of the areas in South America (SA) most

60   vulnerable to the impacts of climate change. The semi-arid conditions in NEB are strongly

61   affected by precipitation variability, and since the 18th century the region has experienced

62   more frequent drought events (Marengo and Bernasconi, 2015; Lima and Magalhães,

63   2018). Today the frequent droughts put ~57 million people, ~27% of the Brazilian

64   population, at risk of experiencing water scarcity (Marengo and Bernasconi, 2015; Lima

65   and Magalhães, 2018). Aside from native people, the region has been occupied since the

66   Portuguese colonization in the 16th century, and the ensuing intense agricultural activity

67   has been responsible for a large-scale degradation of the Caatinga biome, the typical

68   vegetation of NEB's semi-arid areas. This land mismanagement and the increasing

69   frequency of regional droughts has put some of these areas at great risk of desertification

70   (Marengo and Bernasconi, 2015; Sampaio et al., 2020). Advancing our knowledge about

71   NEB's climate and recurrence of extreme events in a long-term context is therefore of

72   great importance to better anticipate the impacts of these intense and abrupt drought

73   events.

74   The Intertropical Convergence Zone (ITCZ) is one of the key elements responsible

75   for precipitation over NEB, which also indirectly affects the South American Summer

76   Monsoon (SASM). When the ITCZ is in its southernmost position during austral autumn,

77   northern areas of NEB experience increased precipitation (Schneider et al., 2014), while

78   the precipitation in the southern areas of NEB occurs mainly during austral summer in

79   response to climatic conditions in the tropical South Atlantic (Vera et al., 2006; Vuille et al.,

3

80   2012). Although these systems are independent and arise in different seasons, the

81   position of the ITCZ affects SASM intensity and its development through moisture influx to

82   the continent (Vuille et al., 2012; Schneider et al., 2014).

83   On orbital to centennial timescales, weakened precipitation in NEB has been

84   associated with enhanced subsidence over NEB during intense SASM periods (Cruz et al.,

85   2009; Orrison et al., 2022), giving rise to a zonal dipole between the western Amazon and

86   NEB (Cruz et al., 2009; Novello et al., 2018). This mode also operates today on

87   interannual and seasonal time scales (Lenters and Cook, 1997; Sulca et al., 2016).

88   More recent studies suggested that these variations on millennial and centennial

89   timescales in NEB may also have been caused by contraction or expansion of the tropical

90   rainbelt affecting the precipitation over South America (Utida et al., 2019; Chiessi et al.,

91   2021). These ITCZ dynamics would be forced by changes in tropical Atlantic and Pacific

92   sea surface temperature (SST) and related atmospheric circulation changes (e.g.,

93   Lechleitner et al., 2017; Utida et al., 2019; Chiessi et al., 2021; Steinman et al., 2022).

94   These results suggest complex ITCZ dynamics operating over NEB; a region where the

95   lack of studies complicates the paleoclimate interpretations for the last millennia.

96   In comparison with the ITCZ, the SASM has received more attention from recent

97   studies, mainly due to its larger area of influence in SA, extending from the tropical Andes

98   to the Amazon and southeastern SA (e.g., Apaéstegui et al., 2018; Azevedo et al., 2019;

99   Della Libera et al., 2022). Rainfall variability over Southern Northeast Brazil (S-NEB) is

100   also determined by the dynamics of the South Atlantic Convergence Zone (SACZ), a

101   component of the SASM (Novello et al., 2018; Zilli et al., 2019; Wong et al., 2021). The

102   spatiotemporal precipitation variability over tropical SA during the Common Era (CE) was

103   evaluated based on a network of high-resolution proxy records (Novello et al., 2018;

104   Campos et al., 2019; Orrison et al., 2022). These studies point to an association between

105 SASM variability and the latitudinal displacement of the ITCZ and SACZ, although

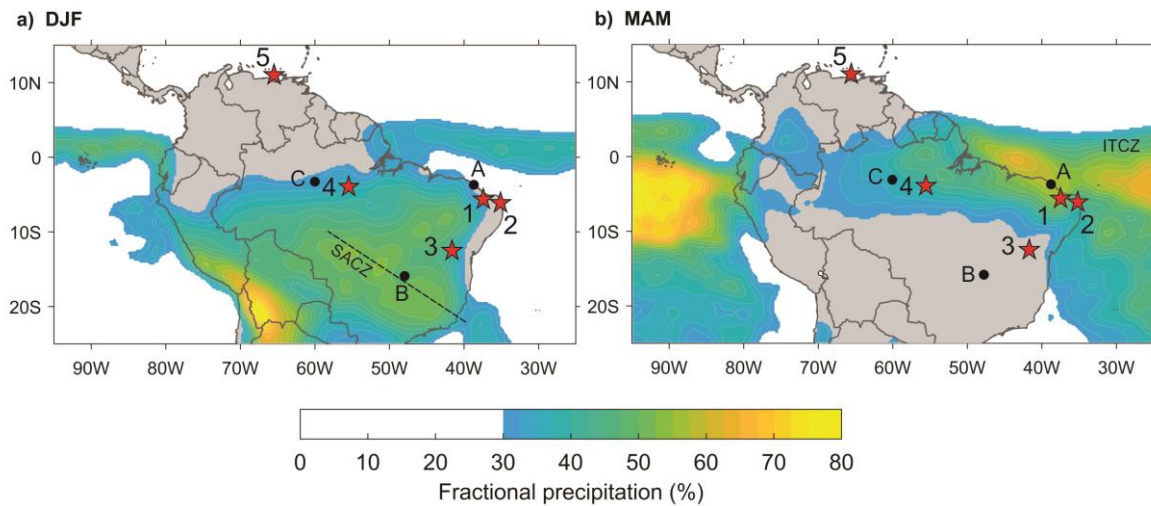106 changes in the latitude of the ITCZ during the last millennia are not well established.

107   Previous studies based on oxygen and hydrogen isotopes from paleorecords

108 obtained in NEB have served as useful proxies for ITCZ precipitation in the region (Cruz et

109 al., 2009; Novello et al., 2012; Utida et al., 2019), while carbon isotopes have been used to

110 interpret soil erosion/production and vegetation cover in different biomes of Brazil (Utida et

111 al., 2020; Azevedo et al., 2021; Novello et al., 2021).

112   For the past 4200 years, NEB has experienced semi-arid conditions (Cruz et al.,

113 2009; Utida et al., 2020) that were imprinted on the oxygen isotope signals recorded in

114 stalagmites. These drier conditions in NEB could have resulted in a seasonal bias toward

115 the δ^{18}O rainfall of recharge periods or an evaporative fractionation of stored karst water

116 (Baker et al., 2019). In addition, isotopic fractionation processes associated with different

117 karst architectures can affect the stalagmites δ^{18}O signals (Treble et al., 2022).

118 Unfortunately, cave monitoring in northern NEB is not available due to the scarcity of

119 dripping water, probably as a result of increasing droughts in the region in the last decades

120 (Marengo and Bernasconi, 2015). Because of this, the interpretation of oxygen isotopes in

121 the region has been challenging.

122   Although the hydrological processes occurring in the epikarst may affect the

123 fractionation of oxygen isotope values in the dripping water and thus control δ^{18}O recorded

124 in stalagmites on a global scale, previous studies mentioned above, suggest a strong

125 relationship with rainfall amount based on model results and comparison with other

126 regional and global records.

127   Building on these recent advances, we present an ITCZ precipitation reconstruction

128 based on stalagmite records from the state of Rio Grande do Norte (RN), located at the

129 modern southernmost limit of the ITCZ in eastern South America (Fig. 1). By using oxygen

130 isotopes obtained from these stalagmites we reconstruct precipitation, based on field

correlations between precipitation amount and oxygen isotopic composition of modern

rainfall, and by using carbon isotopes to reconstruct vegetation/soil cover over the last

3200 years over NEB. These data are essential to fill the gap of high-resolution records in

NEB and to improve the interpretation of ITCZ dynamics over SA and how they are related

to SASM variability during the CE.

Figure 1 – Location and precipitation climatology of study sites during the austral

summer (DJF - December to February) and autumn (MAM - March to May). Color shading

indicates percentage of the annual precipitation total that is received during either DJF or

MAM and highlights the extent of (a) SASM over the continent and (b) the ITCZ over the

ocean. Precipitation data from the Global Precipitation Measurement (GPM) mission, with

averages calculated over the period 2001–2020. 1) Trapiá and Furna Nova Cave, Pedra

das Abelhas Station (this study), 2) Boqueirão Lake (Utida et al., 2019), 3) Diva de Maura

Cave (Novello et al., 2012), 4) Paraíso Cave (Wang et al., 2017), 5) Cariaco Basin (Haug

et al., 2001). GNIP stations: A) Fortaleza, B) Brasília, C) Manaus.

2. Regional settings

2.1. Study area

We study stalagmites from two caves located in the Rio Grande do Norte State, in northern NEB (Fig. 1), Trapiá and Furna Nova Cave. The caves were developed in the Cretaceous carbonate rocks of the Jandaíra Formation, Potiguar Basin, close to the Apodi River valley in a region of exposed karst pavements (Pessoa-Neto, 2003; Melo et al., 2016; Silva et al., 2017). We collected speleothems in Trapiá and Furna Nova caves. Trapiá Cave (5°33'45.43"S, 37°37'15.92"W) is a 2330 m long cave with 29 m of bedrock above the cave cavity. This cave is located 90 km from the Atlantic coast and ~ 50 m above sea level, with temperature and relative humidity of 28.5°C and 100%, respectively, in the chamber. Furna Nova Cave (5°2'3.22"S, 37°34'16"W) is located 60 km north of Trapiá Cave, 45 km from the Atlantic coast and ~95 m above sea level. The cave is 239.3 m long, with 29.8 m of bedrock above the cave cavity. Its temperature and relative humidity in the speleothem chamber are 25°C and 95.0%, respectively.

The annual mean temperature in the region is around 28ºC (INMET - National Institute of Meteorology – Instituto Nacional de Meteorologia – data from 1961-1990) and the average precipitation is approximately 730 mm/year, concentrated in the period between March and May, during the southernmost position of the ITCZ (Agência Nacional de Águas – ANA - National Agency of Waters, 2013; Ziese et al., 2018). Caatinga dry forest is the typical vegetation of the region. It is adapted to short rainy seasons of 3 to 4 months in length and tolerates large interannual variations in precipitation. It is characterized by sparse dry forest, dominated by arboreal deciduous shrubland (Erasmi et al., 2009).

2.2. Climatology

The drylands of NEB extend from 2.5°S to 16.1°S, and from 34.8°W to 46°W, with an area of about 1,542,000 km^2, representing 18.26% of the Brazilian territory (Marengo

175 and Bernasconi, 2015). Although the whole area is classified as semi-arid and has faced

176 intense droughts, especially influenced by El Niño, there are significant differences in

177 climatic systems between the northern and southern sectors of NEB. Furthermore, the

178 NEB eastern coastal sector is characterized by a different rainfall seasonality, receiving

179 more rainfall across the year, as the climate in this region is modulated by the sea breeze

180 circulation and easterly wave disturbances during June and July (Gomes et al., 2015;

181 Marengo and Bernasconi, 2015; Utida et al., 2019). Northern NEB (N-NEB), where the

182 studied caves are located, receives most of its precipitation from March to May, when the

183 seasonal migration of the ITCZ reaches its southernmost position around 2°N (Schneider

184 et al., 2014; Utida et al., 2020), and ITCZ-related precipitation extends across the equator

185 southward to NEB (Fig. 1). In Southern-NEB (S-NEB), the precipitation occurs mainly

186 during summer, from December to February influenced by the margins of the SACZ (Fig.

187 1a).

188

189 *3. Materials and Methods*

190   The rainfall patterns over the study area were evaluated by analyzing monthly

191 rainfall data from the Pedra das Abelhas National Agency of Water (ANA) Station – RN,

192 located ~ 1 km from the Trapiá Cave (Fig. 1), using data from 1911 to 2015 (n=103). In

193 order to exclude possible extreme events with a known forcing, we excluded the 39 El

194 Niño - Southern Oscillation (ENSO) years that most drastically changed the precipitation

195 amount in NEB, following the methodology of Araújo et al. (2013).

196   In order to identify spatial patterns of rainfall associated with the oxygen isotope

197 signal in northeast and central Brazil, we produced maps showing the Pearson's

198 correlation scores between GPCC gridded precipitation anomalies (Schneider et al.,

199 2011), based on the period 1961-1990 for December to February (DJF) and March to May

200 (MAM) (Ziese et al., 2018); and $\delta^{18}O$ values for IAEA-GNIP stations (International Atomic

201 Energy Agency - Global Network of Isotopes in Precipitation, IAEA-WMO, 2021) for

202 Northern NEB (Pedra das Abelhas ANA and Fortaleza GNIP Station); Southern NEB

203 (Andaraí ANA and Brasília GNIP stations) and the Eastern Amazon (Belterra ANA and

204 Manaus GNIP stations). The IAEA stations were chosen based on their closest proximity

205 to sites discussed in the study: 1) Trapiá Cave and Furna Nova Cave (this study), 2)

206 Boqueirão Lake (Utida et al., 2019), 3) Diva de Maura Cave (Novello et al., 2012) and 4)

207 Paraíso Cave (Wang et al., 2017). Sites 1 and 2 are located in in N-NEB, 3 in S-NEB and

208 4 in the Eastern Amazon. Four stalagmites were collected in N-NEB caves, two at Trapiá

209 Cave, TRA5 and TRA7 that are 178 and 270 mm long, respectively (Fig. S1), and two at

210 Furna Nova, FN1 and FN2, with a length of 202 and 95 mm, respectively (Fig. S2). The

211 stalagmite FN1 was previously studied by Cruz et al. (2009) for chronology and oxygen

212 isotopes. Utida et al. (2020) also studied TRA7 for chronology and carbon isotopes.

213 Chronological studies on speleothems were based on U-Th geochronology

214 performed at the Laboratories of the Department of Earth and Environmental Sciences,

215 College of Science and Engineering, University of Minnesota (USA), and at the Isotope

216 Laboratory of the Institute of Global Environmental Change, Xi'an Jiaotong University

217 (China), according to Cheng et al. (2013). Subsamples of ~100 mg were obtained in clear

218 layers, close to the growth axis trying to keep a maximum thickness of 1.5 mm, 10 mm

219 wide and no more than 3 mm depth. The powder samples were dissolved in 14 N HNO_3

220 and spiked with a mixed solution of known ^{233}U (0.78646 ± 0.0002 pmol/g) and ^{229}Th

221 (0.21686 ± 0.0001 pmol/g) concentration. Th and U were co-precipitated with FeCl and

222 separated with Spectra/Gel® Ion Exchange 1x8 resin column with 6N HCl and super clear

223 water, respectively. Th and U were counted in an inductively coupled plasma-mass

224 spectrometry (MC-ICP-MS Thermo-Finnigan NEPTUNE PLUS) and the results calculated

225 in a standard spreadsheet based on Edwards et al. (1987) and Richards and Dorale

226 (2003) using the isotopic ratios measured, machine parameters and corrections factors to

227 eliminate effects of contamination by detrital Th to finally obtain the age of each sample.

228 The decay constants used are: λ_{238} 1.55125 x 10^{-10} (Jaffey et al., 1971), λ_{234} 2.82206 x 10^{-}

229 ^{6} and λ_{230} = 9.1705 x 10^{-6} (Cheng et al., 2013). Corrected ^{230}Th ages assume the initial

230 ^{230}Th/^{232}Th atomic ratio of 4.4 ± 2.2 x 10^{-6}. Those are the values for a material at secular

231 equilibrium, with the bulk earth ^{232}Th/^{238}U value of 3.8 (McDonough and Sun, 1995). The

232 ages are reported in BP (Before Present, defined as the year 1950 A.D.) and also

233 converted to Common Years (CE) and age uncertainties are 2 σ. We analyzed a large

234 number of U/Th ages to improve the age model and reduce the errors associated with

235 detrital Th and recrystallization.

236 Age models of speleothem TRA5 and FN2 were based on 12 and 10 U/Th dates,

237 respectively (Table S1 and S2). The FN1 chronology is based on 10 previously published

238 U/Th results obtained by Cruz et al. (2009) plus 8 additional new dates obtained for this

239 study (Table S1). Speleothem TRA7 has 27 U/Th ages that were presented in Utida et al.

240 (2020). The individual age models for all speleothems were constructed by the software

241 COPRA (Breitenbach et al., 2012) through a set of 2000 Monte Carlo simulations, where a

242 random age within the ±1 σ age interval was chosen each time.

243 For oxygen and carbon isotope analysis of the speleothems, around 200 μg of

244 powder was drilled for each sample, consecutively at intervals of 0.1 mm (TRA5), 0.3 mm

245 (TRA7) and 0.15 mm (FN2), with a Micromill micro-sampling device. These samples were

246 prepared using an online automated carbonate preparation system and analyzed by a

247 GasBench interfaced to a Thermo Finnigan Delta V Advantage at the Laboratory of Stable

248 Isotopes (LES) at the Geoscience Institute of the University of São Paulo. Isotopes are

249 reported in delta notation (δ^{18}O and δ^{13}C) relative to the Vienna Pee Dee Belemnite

250 (VPDB) standard, with uncertainties in the reproducibility of standard materials < 0.1 ‰.

251 The isotopic profiles of TRA5, TRA7, FN1 and FN2 stalagmites consist of 443, 885, 1215

252 and 651 isotope samples, respectively. These datasets provide an average resolution of

253 ~1 year per sample for TRA5 and ~ 4 years for the other speleothem records. TRA7 δ^{13}C

254 results were presented by Utida et al. (2020) and FN1 δ^{18}O results by Cruz et al. (2009)

255 using the same methods. Cruz et al. (2009) do not provide FN1 δ^{13}C results, which were

256 not included in this study.

257 Different textural characteristics of speleothem TRA5 and FN2 were identified in

258 intervals which were analyzed for mineralogical composition based on approximately 20

259 mg samples with X-ray powder diffraction in a Bruker D8 diffractometer (Cu Kα, 40 kV, 40

260 mA, step 0.02°, 153 s/step, scanning from 3 to 105° 2θ) at the NAP Geoanalítica

261 Laboratory of the University of São Paulo. Qualitative and quantitative mineralogical

262 analyses were performed with *Match!* and *FullProf* software, using the Crystallographic

263 Open Database (Grazulis et al., 2009). Crystallographic data for the mineral phases were

264 taken from Pokroy et al. (1989) for aragonite and from Paquette and Reeder (1990) for

265 calcite. Mineralogical results of TRA7 and FN1 were obtained by Utida et al. (2020) using

266 the same method. All results are presented in weight proportion (wt %). The δ^{18}O results of

267 speleothems were calibrated according to the percentage of calcite identified for the

268 interval applying the aragonite–calcite fractionation offset of 0.85 ‰ ± 0.29 ‰ (Zhang et

269 al., 2014). The δ^{13}C results were not corrected because the original aragonite–secondary

270 calcite fractionation factor is negligible (~0.1-0.2 ‰) (Zhang et al., 2014). Even considering

271 the original aragonite-original calcite mean fractionation factor of 1.1 ‰ (Zhang et al.,

272 2015), the range of δ^{13}C RN stalagmites is very large (>8 ‰) and the correction would not

273 affect the main interpretation.

274 The intra-site correlation model (*iscam*) was used to construct a composite record

275 (Fohlmeister, 2012). It combined the climate records to obtain a unique age model and

276 oxygen isotopic record, corrected only for mineralogical composition of speleothems from

277   Rio Grande do Norte, which here is referred to as the RN Composite. The age-depth

278   modeling software was adjusted to calculate 1000 Monte-Carlo simulations on absolute

279   age determinations to find the best correlation between oxygen isotope records from

280   Trapiá and Furna Nova speleothems, reproducing adjacent archives. The results estimate

281   the error of the age-depth model by indicating the 68 %, 95 % and 99 % confidence

282   intervals obtained from evaluation of a set of 2000 first order autoregressive processes

283   (AR1) for each record (Table S3). This method allows significantly reducing the age

284   uncertainty within the overlapping periods and it can be tested if the signal of interest is

285   indeed similar in all the records (Fohlmeister, 2012). The age data were assumed to have

286   a Gaussian distribution and were calculated pointwise. The composite result was

287   detrended and normalized, according to the *iscam* method. The performance of the *iscam*

288   results is affected by low quality of chronological control, low resolution and hiatuses.

289   Therefore, the following intervals were removed from the stalagmite records before

290   constructing the RN Composite: FN1 0-12 mm and 187-202 mm, FN2 0-6 mm, TRA5 0-37

291   mm and TRA7 222-227 mm. In addition, the FN1 record was divided into two portions:

292   FN1a 12.14-136.99 mm and FN1b 140.15-186.87 mm that are separated by a hiatus. The

293   chronological age-depth relationship in the overlapping parts of the individual stalagmites

294   was modified and improved according to the *iscam* results of the composite record. The

295   composite calculation rearranges the proxies in order to obtain the optimal calculated age

296   and then calculates the average of the proxy data after normalizing the records. The RN

297   record only contains overlapping segments between two stalagmites per period. Hence the

298   RN composite proxy error can be quantified as the difference between the δ^{18}O of the

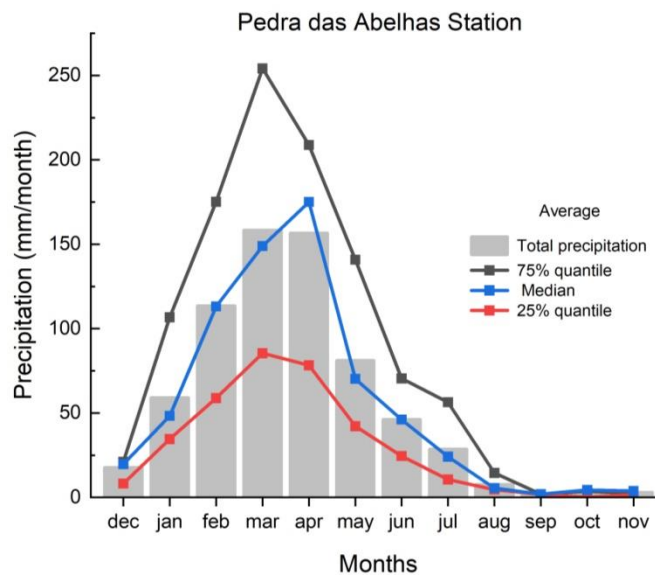299   stalagmites combined for any given point in time (Fig. S6).

300

301   *4. Results*

302   *4.1. Modern climatology and δ^{18}O rainfall distribution*

303   The data from Pedra das Abelhas Station reveal that in the majority of years

304   (normal years - interquartile range) the rainy season persists from February to April, with

305   precipitation varying from 100 to 180 mm/month, and minor contributions occurring in

306   January and May (50-70 mm/month) (Fig. 2). During the drier years (lower quartile),

307   February has a reduced precipitation amount, similar to the amount in January during

308   normal years, as described above. The maximum precipitation of 90 mm/month occurs

309   between March and April. For wetter years (upper quartile), the rainy season starts in

310   January with more than 100 mm/month and lasts until May with almost 150 mm/month,

311   reaching values higher than 250 mm around March. These data show that wetter years

312   are characterized by increased precipitation amounts and a longer rainy season starting in

313   January and ending in May, while the precipitation deficit during drought years is a result

314   of decreased precipitation amount and a shorter rainy season, with a peak in precipitation

315   between March and April. The anomalous length of the rainy season during dry and wet

316   years is attributed to variations in the meridional SST gradient in the tropical Atlantic that

317   results in a shift of the ITCZ to the north or south of its climatological position (e.g.,

318   Andreoli et al., 2011; Marengo and Bernasconi, 2015; Alvalá et al., 2019).

319   In S-NEB, the precipitation occurs mainly during summer, from December to

320   February (Fig. 1a and 3b). This regional seasonality difference with N-NEB is evident in

321   the spatial correlation map between GPCC precipitation anomalies and δ^{18}O anomalies

322   obtained from IAEA-GNIP for Fortaleza and Brasília stations (Fig. 3). The reddish areas on

323   the map indicate significant negative correlations during the austral summer (DJF) and

324   autumn (MAM) between the local precipitation δ^{18}O signals and the regional precipitation

325   amount. Overall, the spatial correlations indicate that in both areas the amount effect is the

326   dominant effect on the isotopic composition of rainfall (Dansgaard, 1964). However, the

327   isotopic signal varies seasonally and as a function of the two different circulation systems.

328   The negative spatial correlation observed over N-NEB (Fig. 3a) suggests precipitation is

329　dominated by ITCZ dynamics, similar to the conditions over Fortaleza, while the negative

330　spatial correlation over S-NEB (Fig. 3b) is a result of the rainfall influenced by the SASM

331　(Fig. 1) (Vera et al., 2006), such as in Brasília City, in central Brazil. Therefore,

332　precipitation and the associated isotopic signal are the result of ITCZ dynamics in N-NEB,

333　while they are influenced by the SASM in the S-NEB. Accordingly, their rainfall seasonality

334　is also different (Fig. 3), with a NDJFM peak in the south (Brasília, Fig. 3b) and a MAM

335　rainfall peak in the north (Fortaleza, Fig. 3a).

336

337

338　　　Figure 2 - Pedra das Abelhas ANA Station precipitation analyzed from 1911 to

339　2015 (n= 103), excluding the strongest ENSO years (39 years), according to Araújo et al.

340　(2013).

341

342　　　Another important region in SA affected by the ITCZ behavior is the eastern

343　Amazon, west of the NEB (Fig. 1 and Fig. 3c). This region is characterized by increased

344　precipitation during DJFMAM and a peak in rainfall and $\delta^{18}O$ minimum in MAM (Fig. 3c) as

345　a result of precipitation received from the ITCZ in both summer and autumn. It can be

346　depicted by the negative correlation between $\delta^{18}O$ at the Manaus GNIP station and rainfall

14

over the upstream equatorial region under direct ITCZ influence. In addition, there is only a minor influence through water recycling over the Amazon Basin, due to its proximity to the coast (Wang et al., 2017).

Figure 3 – Monthly mean observed precipitation amount collected at ANA and δ^{18}O values for GNIP stations (IAEA-WMO, 2021) (black dots) and correlation maps between gridded precipitation and δ^{18}O anomalies from the same stations (black dots) for: (a) Northern NEB, Fortaleza and Pedra das Abelhas stations (star 1), (b) Southern NEB, Brasília and Andaraí stations (star 3), c) Eastern Amazon, Manaus and Belterra stations

357 (star 4). The maps show the spatial correlation between δ^{18}O anomalies at GNIP stations

358 and GPCC gridded precipitation anomalies based on the period 1961-1990 for December

359 to February (DJF) and March to May (MAM) for Fortaleza, Brasília and Manaus stations

360 (Ziese et al., 2018). The δ^{18}O values (left *y* axis) and precipitation (right *y* axis) for each

361 station were obtained from GNIP IAEA/WMO database. Stars indicate the site locations: 1)

362 Trapiá Cave, Furna Nova Cave and Pedra das Abelhas ANA Station (reference period

363 1910-2019), 2) Boqueirão Lake (Utida et al., 2019), 3) Diva de Maura Cave (Novello et al.,

364 2012) and Andaraí ANA Station (reference period 1960-1986), 4) Paraíso Cave (Wang et

365 al., 2017) and Belterra ANA Station (reference period 1975-2007), 5) Cariaco Basin (Haug

366 et al., 2001).

367

368 *4.2. Chronology and mineralogy*

369 The RN record covers the last 5000 years, four stalagmites cover the last 3250

370 years, and two of these stalagmites cover partially the time period between 3000 and 1260

371 Before Common Era (BCE), with the exception of one hiatus at 2100 -1720 years BCE

372 (Fig. 4, Table S1 and S2).

373 Stalagmite TRA7 from Trapiá Cave was deposited from 3000 to 2180 BCE (Fig.

374 S3) with a low deposition rate (DR) of approximately 0.05 mm/yr. After a hiatus of 1880

375 years, it resumed deposition from 300 BCE until 1940 CE with a DR of 0.18 mm/yr. The

376 TRA5 stalagmite deposition occurred continuously from 1490 to 1906 CE (Fig. S3) with a

377 DR of 0.33 mm/yr.

378 Stalagmite FN1 from Furna Nova was deposited over the last 3600 years, with a

379 hiatus from 125 to 345 BCE and another one of approximately 100 years between 1525

380 and 1662 CE (Fig. S3), with an average DR of 0.09 mm/yr. The ages from the FN1

381 stalagmite are all in chronological order and contain low errors and were therefore all kept

382   in the age model. The FN2 stalagmite deposited continuously from 1226 BCE to 7 CE,

383   except for a hiatus between 189 and 45 BCE (Fig. S3) with a DR of 0.20 mm/yr.
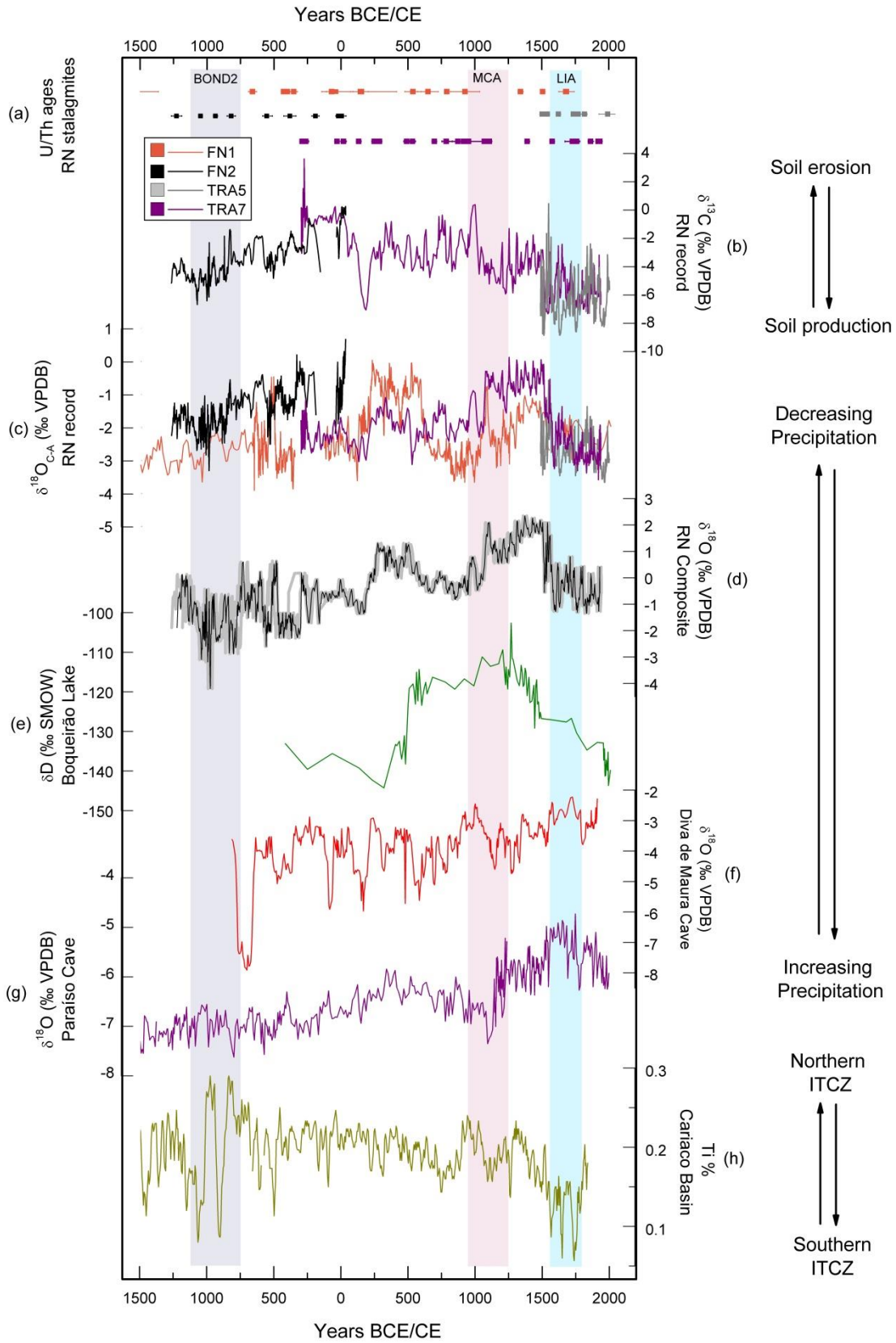
384   The mineralogy of the stalagmites from Trapiá Cave is formed by layers of crystals

385   with mosaic and columnar fabrics, composed exclusively of calcite, except for the base

386   portion of TRA7 from 173 to 270 mm (3000 BCE to 130 CE), which is described as an

387   interbedded needle-like crystals texture, composed of 87.1 to 99% of aragonite (Fig. S1,

388   Table S4). The same needle-like morphology is present in most of the Furna Nova Cave

389   stalagmites, composed of aragonite with a weight proportion greater than 85 % in FN1,

390   extending from 0 to 83 mm (160 to 1340 CE) and from 128 to 183 mm (1730 BCE to 80

391   CE). In the FN2 sample this weight proportion is greater than 93.4 % (1265 BCE to 35

392   CE). The only interval composed of 100 % calcite is from 95 to 125 mm in FN1 (Fig. S2,

393   Table S4). These speleothem samples show no sign of dissolution or recrystallization.

394

395   *4.3. Stalagmite $\delta^{18}O$ and $\delta^{13}C$*

396   The oxygen isotope ratios of the RN record vary from 0.6 ‰ to -4.5 ‰, with $\delta^{18}O$

397   mean values for each speleothem of -2.8 ‰ for TRA7, -3.5 ‰ for TRA5, -2.4 ‰ for FN1

398   and -1.5 ‰ for FN2. Similarities among the stalagmites are evident, especially around

399   1500 CE when $\delta^{18}O$ values abruptly decrease in TRA7 and TRA5, while in FN2 this period

400   features a hiatus (Fig. S4).

401   The $\delta^{18}O$ correction due to mineralogy for the stalagmites from Furna Nova Cave

402   resulted in changes of less than 0.1 ‰ of their mean values. The mean correction for

403   TRA7 equals an enrichment of 0.5 ‰ during the period spanning 130 BCE to 1940 CE.

404   Values from TRA5 were corrected along the entire sample by adding 0.85 ‰, as it is

405   composed of 100 % calcite. Therefore, the mean values increased from -3.5 ‰ to -2.7 ‰

406   (Fig. S4).

408   Figure 4 – Rio Grande do Norte stalagmite isotope records and comparisons with

409   other records from South America. a) U/Th ages from each stalagmite studied. b) Raw

410   data of δ^{13}C. c) Oxygen isotope results corrected for calcite-aragonite fractionation (δ^{18}O$_{C-}$

411     $_A$), according to weight proportion of mineralogical results. d) δ^{18}O RN Composite

412   constructed using stalagmite records from NEB (black line). Grey shaded area denotes the

413   99 % confidence interval of the age model. Blue shaded area refers to LIA (Little Ice Age),

414   pink shaded area refers to MCA (Medieval Climate Anomaly), light grey shaded area

415   refers to Bond 2 event. e) Boqueirão Lake δD record (Utida et al., 2019). f) DV2

416   speleothem oxygen isotope record from Diva de Maura cave, southern NEB (Novello et

417   al., 2012). g) PAR01 and PAR03 δ^{18}O records from Paraíso cave, eastern Amazon (Wang

418   et al., 2017). h) Ti record of Cariaco Basin (Haug et al., 2001).

419

420   Four main phases describe the δ^{13}C dataset (Fig. 4b). The oldest phase from 3000

421   to 2160 BCE is characterized by δ^{13}C values close to zero. After a hiatus (2170-1270 BCE)

422   there is a short interval of stability with δ^{13}C values around -4 ‰ that lasts from 1270 to

423   840 BCE and is followed by a δ^{13}C enrichment that reaches a value of zero at 30 CE.

424   Between 30 and 1500 CE there is a trend toward more negative δ^{13}C values, varying from

425   0 to -8.8 ‰. This interval is marked by a valley at 190 CE with δ^{13}C values of -7.2 ‰ and a

426   peak at 1000 CE with δ^{13}C values of 0.22 ‰. The youngest period, from 1500 to 1930 CE

427   is more stable than the previous one, with δ^{13}C values averaging around - 6.4 ‰.

428

429   *4.4. Composite*

430   Combining the δ^{18}O results from the four RN stalagmites allows establishing a

431   continuous record covering the last ~3200 years, the RN Composite (Fig. 4d). The

432   correlation coefficient (r) between each measured δ^{18}O stalagmite time series is >0.59,

433   significant at the 95 % level (Fig. S5). The composite provides an average temporal

434   resolution of ~2 years. The entire stable isotope time series is composed of 2495 δ^{18}O

435   measurements, corrected according to mineralogical composition.

436

437   *5. Discussion*

438   *5.1. U/Th chronology and RN Composite*

439   The high values of ^{232}Th and low ^{230}Th/^{232}Th ratio suggest incorporation of detrital

440   Th transported by the seepage solution to the speleothems, which lead to a higher

441   uncertainty of the age values. Recrystallization of aragonite into calcite might also reduce

442   the U content and given older ages for carbonates (Lachniet et al., 2012). We assume that

443   these are the main reasons for age inversions along speleothems from Northeast Brazil.

444   Because FN1 is mostly composed of aragonite and presents low U concentration in

445   some samples of the first 127 cm and high ^{232}Th amounts, we considered the association

446   of low ^{230}Th/^{232}Th and low U content the most important factor affecting the age errors and

447   inversions in the FN1 stalagmite. In contrast, the FN2 stalagmite has a more precise

448   chronology due to the predominant aragonite composition, with high ^{238}U content and

449   higher ^{230}Th/^{232}Th ratio than FN1. Although the TRA5 stalagmite is entirely composed of

450   calcite, the ^{238}U content is relatively high compared to other stalagmites, which improves

451   the confidence in its age results. The high ^{232}Th contamination of TRA5 samples is the

452   main factor attributed to cause age inversions and increased errors. According to age

453   results produced by Utida et al. (2020), most of the TRA7 ages are in chronological order

454   and the inversions seem to not have a direct relationship with ^{238}U amount, and the high

455   ^{232}Th content is similar to other ages from TRA7. Most of the TRA7 stalagmite used in our

456   composite is composed of calcite and might not affect the main trends of δ^{18}O.

457   The age uncertainties caused by high ^{232}Th concentration and calcite

458   recrystallization in stalagmites might affect the age model. However the strong coherence

459 between the δ^{18}O curves from different stalagmites argues in favor of the good quality of

460 our chronology. This is evident when FN2, which is composed 100 % of aragonite, is

461 compared with other samples. There is a different amplitude range in its δ^{18}O values, but

462 when the curve is superposed on other δ^{18}O records the variability is similar. This

463 amplitude range is corrected when the δ^{18}O results are submitted to the *iscam* composite

464 construction, since it normalizes the results (Fig. S6).

465 Although the δ^{18}O results present a different range of values between FN2 and

466 FN1, the mineralogical correction did not significantly change the main curves (Fig. S4).

467 TRA7 and FN1 underwent substantial changes due to mineralogical corrections between

468 80 to 1500 CE (Table S4). However the δ^{18}O trends were not modified. The mineralogical

469 correction for the last 500 years, adjusts the δ^{18}O values over the same range for TRA5,

470 TRA7 and FN1 (Fig. S4). Some of this δ^{18}O variability might also be attributed to karst

471 fractionation effects. However, no cave monitoring in northern NEB is available that could

472 quantify the extent of these processes.

473 These differences in mineralogical corrections and possible δ^{18}O fractionations did

474 not alter the general shape of the RN Composite. Before merging the results, *iscam*

475 normalizes the δ^{18}O and different range values are adjusted to the same scale, resulting in

476 significant reduction in the difference between stalagmite records (Fig. S6). The largest

477 error occurs between 250 and 580 CE, when the maximum and minimum values of FN1

478 and TRA7 are 2.4 ‰ and -1.50 ‰ after normalization, respectively (Fig. S6). This is a

479 period when FN1 registers high δ^{18}O values; an anomaly that is not evident in TRA7. The

480 period extending from 500 to 570 CE, is characterized by an anti-phased signal between

481 FN1 and TRA7, and hence the RN Composite shows a smoothed signal during this time.

482

483 *5.2. Paleoclimate interpretation*

484   The variability of the global $\delta^{18}O$ values for speleothems originating from the same

485   cave is ~ 0.37 ‰, which can be attributed to karst fractionation effects and not directly to

486   hydroclimate, host rock geology, cave depth or cave microclimate instability (Treble et al.,

487   2022). Some intervals in coeval RN stalagmites from the same cave are above this limit,

488   however, we demonstrated based on the composite treatment associated with

489   mineralogical corrections that the $\delta^{18}O$ variability from the RN record is similar for

490   stalagmites from the same cave and between the two studied caves throughout the period

491   analyzed, further reinforcing the notion applied by previous studies that these records can

492   be interpreted in a paleoclimatic context (Cruz et al., 2009; Utida et al., 2020). In addition,

493   we consider the RN composite as representative of a precipitation $\delta^{18}O$ signal, since the

494   differences between stalagmite records are significantly reduced after age rearrangements

495   and isotope normalization.

496   The $\delta^{18}O$ RN Composite allowed us to reconstruct precipitation changes influenced

497   by the ITCZ position in N-NEB and its convective intensity. This interpretation is based on

498   the spatial correlation between $\delta^{18}O$ at GNIP stations and GPCC precipitation (Fig. 3).

499   Highest precipitation amounts occur between March and May and they coincide with more

500   depleted $\delta^{18}O$ precipitation signals, consistent with the amount effect (Dansgaard, 1964).

501   Hence, the most negative $\delta^{18}O$ values in RN stalagmites reflect an increased rainfall

502   amount, as a consequence of an ITCZ position close to N-NEB (Cruz et al., 2009; Utida et

503   al., 2019).

504   A generally drier climate prevailed in NEB after the 4.2 ky BP (kiloyear Before

505   Present) event in the Mid-Holocene (Cruz et al., 2009). This led to the development of the

506   Caatinga, a sparse vegetation cover which has persisted in NEB to the present (De

507   Oliveira et al., 1999; Utida et al., 2020; Chiessi et al., 2021). These drier conditions favored

508   soil erosion during rainfall events and reduced soil thickness (Utida et al., 2020). When

509 erosion events remove most of the soil cover, there is an increase in the carbon

510 contribution from local bedrock (mean $\delta^{13}C$ of 0.5 ‰), which leads to higher $\delta^{13}C$ values in

511 the NEB stalagmites from RN. On the other hand, more negative $\delta^{13}C$ values in

512 stalagmites are associated with increased soil coverage and soil production (Utida et al.,

513 2020). In NEB soils have a $\delta^{13}C$ average around -25 ‰, which suggests a dominant

514 influence from C3 plants with $\delta^{13}C$ values ranging between -32 ‰ and -20 ‰ (Pessenda et

515 al., 2010). Therefore, the $\delta^{13}C$ stalagmite results are interpreted as changes in soil

516 production/erosion and the density of vegetation coverage (e.g., Utida et al., 2020;

517 Azevedo et al., 2021; Novello et al., 2021).

518   The oldest period covered by the RN Composite, from 1200 to 500 BCE, is

519 characterized by successive dry and wet multidecadal periods, with increased precipitation

520 in N-NEB from 1060 to 750 BCE and from 460 to 290 BCE, as suggested by the negative

521 departures seen in the $\delta^{18}O$ values. During this last period, there is also a tendency from

522 lower to higher $\delta^{13}C$ values, suggesting progressive surface soil erosion related to rainfall

523 variability (Fig. 4), as interpreted by Utida et al. (2020). This period ends up in a stable

524 interval, lasting from 300 BCE to 0 CE, with little fluctuation in $\delta^{18}O$ values and $\delta^{13}C$ values

525 close to the bedrock signature at about -1 ‰ to +1 ‰, indicating a lack of soil above the

526 cave. After an abrupt reduction of both isotopes around 200 CE, there was a brief time of

527 increased precipitation and vegetation development. Between 200 CE and 1500 CE,

528 decreased $\delta^{13}C$ values, reaching approximately -2 ‰, suggest a vegetation development

529 above the cave. However, $\delta^{18}O$ values indicate significant variability with two main periods

530 of dry conditions, from 270 to 530 CE and 1060 to 1500 CE. From 1500 CE to the present,

531 more negative values of $\delta^{18}O$ represent wetter climatic conditions. The more negative $\delta^{13}C$

532 during this period can be related to denser vegetation that favored both soil production and

533 stability above the cave. Due to the high range of $\delta^{13}C$ results (more than 11 ‰), we

23

assume that the Prior Calcite Precipitation effect is negligible in our results. In addition, a more positive δ^{13}C signal occurs around 280 BCE when the climate conditions were not the driest in the last 5000 years, thus probably representing a local environmental change.
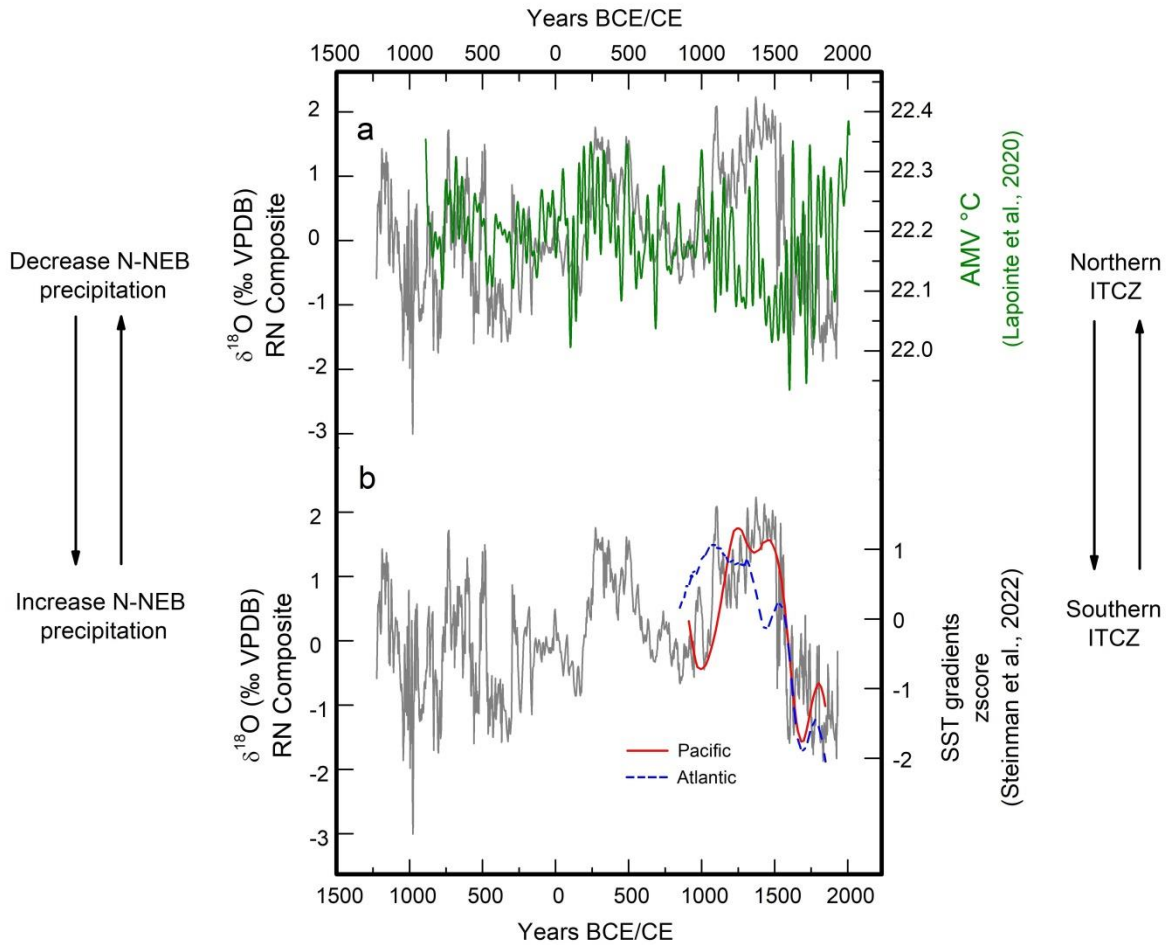
During the last 2500 years, the RN Composite shows similar characteristics as the lower-resolution δD lipids record (n-C28 alkanoic acid from leaf waxes) obtained in Boqueirão Lake sediments (N-NEB) (Figs. 1 and 4). Both records show a more stable climatic signal between 400 BCE and 350 CE. From 500 to 1500 CE, enriched δD lipids obtained in Boqueirão Lake were interpreted as the beginning of a long dry phase (Utida et al., 2019), although the beginning of the dry period is slightly delayed when compared with the RN speleothem isotope record. This inconsistency might be related to different chronological controls between lake and stalagmite records and possibly also by the location of Boqueirão Lake that is affected by the ITCZ and winter breezes as it is located in the eastern coastal sector of NEB (Zular et al., 2018; Utida et al., 2019).

It is important to note that the RN record exhibits a climatic signal that is distinctly different from the from DV2 speleothem record from Diva de Maura Cave in S-NEB (Novello et al., 2012). Although both regions are affected by the same mesoscale atmospheric circulation, the RN site receives its precipitation directly from the ITCZ. At the S-NEB site, on the other hand, the primary source of precipitation is associated with the monsoon, as it is located too far inland to be affected directly by the ITCZ, as demonstrated by the correlations maps (Fig. 3). The general trend toward more positive values, as a result from insolation forcing, occurs from 150 to 1500 CE in the RN Composite, but from 600 to 1900 CE in the DV2 sample (Cruz et al., 2009; Novello et al., 2012). This trend is a result of the persistent dry conditions in the entire NEB region that suggests an ITCZ contraction in an orbital timescale, resulting in drier conditions over NEB during periods of maximum austral summer insolation (Cruz et al., 2009; Chiessi et al., 2021; Campos et al., 2022). However, the DV2 record does not document the same

24

560   multidecadal and centennial-scale climate variability as recorded in the RN speleothem

561   record, nor the less dry interval from 600 to 1060 CE seen in the RN Composite (Fig. 4).

562   As demonstrated by the spatial correlation maps between $\delta^{18}O$ values and regional

563   precipitation (Fig. 3), the S-NEB and N-NEB regions are influenced by distinct rainfall

564   regimes whose peaks of precipitation arise during the summer monsoon season and the

565   autumn ITCZ, respectively. Our data provide evidence for a spatial and temporal

566   distinction of NEB climate patterns for the past that can be interpreted as differences in

567   seasonality during the last millennia. Furthermore, contemporaneous dry or wet events in

568   both N-NEB and S-NEB suggest the occurrence of larger regional climate changes with

569   higher environmental impacts.

570   When comparing N-NEB and eastern Amazon conditions, it is evident that the RN

571   Composite shares some similarities with the Paraíso stalagmite record (Wang et al.,

572   2017), due to the contribution of ITCZ precipitation in both places. But there are also

573   important differences (Fig. 4). The RN Composite shows lower $\delta^{18}O$ values between 500

574   and 1000 CE, compared to the earlier period, while Paraíso shows gradually decreasing

575   values around the same period, suggesting a slight increase in precipitation in both areas.

576   From 1160 to 1500 CE, abrupt increases in $\delta^{18}O$ values are seen in both records, which

577   indicate abrupt and prolonged drought conditions due to a northward ITCZ migration.

578   However, around 1100 CE, centered in the MCA, and the period from 1500 to 1750 CE,

579   Paraíso is antiphased with the RN Composite and in phase with the Cariaco Basin (Haug

580   et al., 2001), which is inconsistent with the notion of an ITCZ-induced regional precipitation

581   change. Instead, a zonally-oriented precipitation change within the ITCZ domain over

582   Brazil is required to explain the anti-phased behavior between precipitation in N-NEB and

583   the eastern Amazon, and similarities between Cariaco and the eastern Amazon.

584   We investigate the potential relationship between $\delta^{18}O$ values in our RN

585   speleothems and an ITCZ displacement toward the warmer hemisphere to explain

586   paleoclimate variability observed in N-NEB. In order to test this hypothesis, the RN

587   Composite was compared with a reconstruction of Atlantic Multidecadal Variability (AMV)

588   (Lapointe et al., 2020) (Fig. 5). Some studies suggest that the warm phase of the AMV

589   (when the North Atlantic presents warm SST) forces the mean ITCZ to shift to the north of

590   its climatological position, thereby causing a reduction in NEB rainfall (Knight et al., 2006;

591   Levine et al., 2018), while a recent study suggests that the warm phase of the AMV would

592   cause a weakening of the ITCZ from February to July (Maksic et al., 2022). The driest

593   periods from 750 to 500 BCE, 200 to 580 CE and 1100 and 1500 CE occurred during long,

594   relatively warm AMV anomalies. The warm average temperature of 22.19° C for the

595   period, would force a northward ITCZ displacement or an ITCZ weakening, and in both

596   cases the result is low precipitation over NEB. The lowest AMV temperature (cold phase)

597   around 1500 CE might be related to the abrupt dry conditions seen in the RN Composite

598   and suggests an increased equatorial Atlantic SST, and consequently increased

599   precipitation over N-NEB (Fig. 5). Opposite conditions between the RN Composite and the

600   AMV can be observed during the Current Warm Period, which requires further

601   investigation. The relationship between North Atlantic temperature and ITCZ location can

602   also explain the Bond 2 Event recorded in the RN Composite. It is marked by increased

603   precipitation around 1000 BCE, when the ITCZ was displaced toward the south. This

604   southerly ITCZ displacement might be attributed to persistently lower temperatures in the

605   North Atlantic (Bond et al., 2001; Broccoli et al., 2006) caused by the slowdown of the

606   Atlantic Meridional Overturning Circulation (Jackson et al., 2015).

607

Figure 5 - δ^{18}O RN Composite compared with (a) Atlantic Multidecadal Variability (Lapointe et al., 2020) and (b) Pacific and Atlantic Sea Surface Temperature gradients calculated (z-score) according to Steinman et al. (2022). Atlantic: 2 σ range of 1000 realizations of the Atlantic meridional SST gradient (north – south). Pacific: median of 1000 realizations of the Pacific zonal SST gradient (west – east).

613

Steinmann et al. (2022) suggested a southward displacement of the ITCZ during the Common Era toward the southern hemisphere in response to changes in the Pacific and Atlantic meridional SST gradients. Indeed, our RN Composite is dynamically consistent with these SST gradient changes and in agreement with the hypothesis of a north-south oscillation of the latitudinal ITCZ position in the tropical Atlantic during the last

619   millennia, modulating precipitation over N-NEB. When the tropical South Atlantic and

620   tropical eastern Pacific are anomalously warm – negative z-score (cold - positive z-score)

621   (Fig. 5) the ITCZ is displaced to the south (north), resulting in increased (decreased)

622   precipitation over NEB. The abrupt changes in N-NEB precipitation around 1100 and 1500

623   CE occur approximately synchronous with the SST gradient changes, confirming how

624   sensitive the RN speleothems respond to changes in the ITCZ latitudinal position (Fig. 5).

625   The same is observed during the period equivalent to the LIA, between 1560 and 1800 CE

626   considering N-NEB, S-NEB and eastern Amazon records, when both Pacific and South

627   Atlantic became warmer (Fig. 5). According to Steinmann et al. (2022), during the LIA

628   period warm SST in the eastern tropical Pacific and in the tropical South Atlantic would

629   promote a southward displacement of the ITCZ. This is supported by other records from

630   the western Amazon and the tropical Andes that document an intensified SASM during the

631   LIA, fueled by the southern location of the ITCZ (e.g., Vuille et al., 2012; Apaéstegui et al.,

632   2018), which is also very well recorded in other archives around the tropics (Leichleitner et

633   al., 2017; Campos et al., 2019; Orrison et al., 2022; Steinmann et al., 2022).

634   According to Kayano et al. (2020, 2022), during the last century, dry conditions

635   over N-NEB and the eastern Amazon are present when AMV and Pacific Decadal

636   Variability (PDV) are both in their warm phases, or when the AMV is in a cold phase and

637   the PDV in its warm phase. On the other hand, when AMV and PDV are both in their cold

638   phase, precipitation over the Amazon is anti-phased with NEB, resulting in decreased

639   precipitation over the Amazon and increased precipitation over NEB. This zonally aligned

640   precipitation signal over eastern tropical South America is the result of joint perturbations

641   of both the regional Walker and Hadley Cell's produced by teleconnection between the two

642   ocean basins (He et al., 2021). This joint interaction between the two basins can help

643   explain the results seen during the cold AMV phase between 1500 and 1750 CE (Fig. 5),

644   when precipitation over N-NEB increased, but the eastern Amazon saw a decrease in

645   precipitation (Fig. 4).

646

647   *5.3. TRA5 δ^{18}O stalagmite and extreme drought events*

648   The last 500 years were the wettest of the last two millennia and the onset of this

649   period was forced by Atlantic and Pacific SST, according to our results (Figs. 4 and 5).
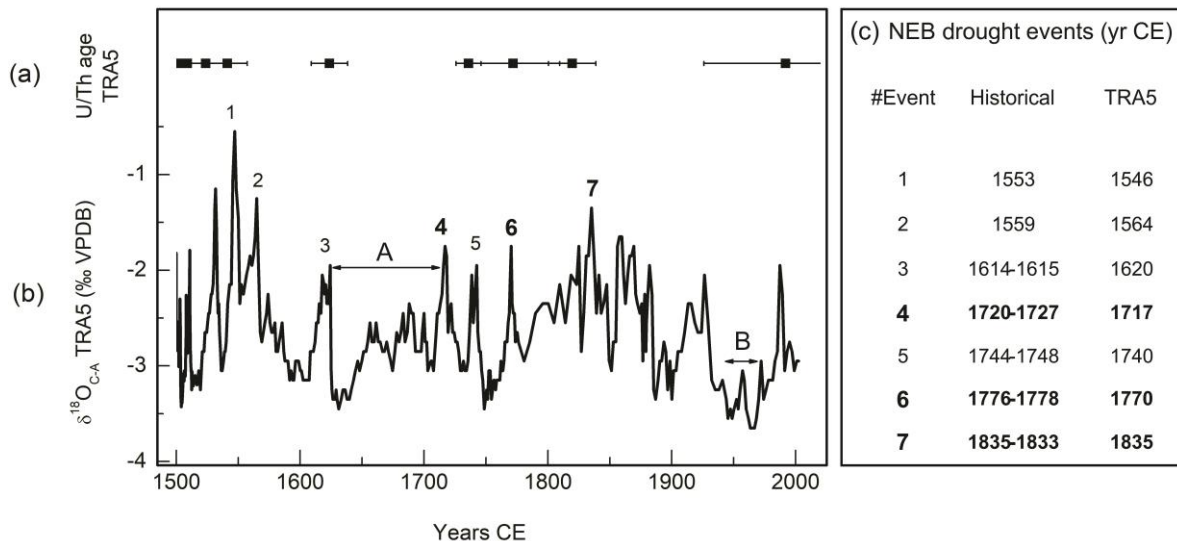
650   Superimposed on these long-term negative δ^{18}O anomalies, distinct peaks are recorded in

651   the TRA5 δ^{18}O record from 1500 to 1850 CE (Fig. 6). These drought events are visible in

652   this record thanks to its higher deposition rate (faster growth) and thus higher temporal

653   resolution of the δ^{18}O record when compared to other stalagmites used in our study. No

654   preferred periodicity of these events is apparent in our record, preventing comparison with

655   ENSO events, for example. There exist no precipitation reconstructions or observations

656   from this region between 1500 and 1850 CE, aside from historical drought records.

657

(c) NEB drought events (yr CE)		
#Event	Historical	TRA5
1	1553	1546
2	1559	1564
3	1614-1615	1620
4	**1720-1727**	**1717**
5	1744-1748	1740
6	**1776-1778**	**1770**
7	**1835-1833**	**1835**

658

659   Figure 6 – TRA5 record and equivalent historical record. (a) U/Th age is

660   represented by black dots and horizontal lines indicate age uncertainty. (b) δ^{18}O$_{C-A}$ record,

661   numbers represent the peak of a drought event. Bold numbers represent the most severe

drought events. A - Few drought events interval from 1620 to 1970s period. B - 1940s to 1970s period. (c) Occurrence of historical drought years compiled from Lima and Magalhães (2018).

Although the age model errors of TRA5 are larger and could limit our ability to attribute $\delta^{18}O$ peaks to specific single-year events, it still allows for a comparison between these abrupt events with historical records to demonstrate the long-term context of abrupt drought events in modern human history. We thus consider our speleothem-based record as a first attempt to reconstruct precipitation in Northeast Brazil that would allow for a comparison with historical droughts. If our speleothem records regional hydroclimate, it should retain a signal of the most intense droughts over NEB that are known to have struck the region based on the available historical literature of Brazil.

The highest peaks correspond to extreme drought events, such as the ones centered around 1546 and 1564 CE (points 1 and 2 of Fig. 6). They can be associated with observed historical droughts that took place in 1553 and 1559 CE. These were the first two events recorded in Brazil by the Portuguese Jesuits that led to a reported reduction in riverflow in the tributaries of the main rivers of NEB (Serafim Leite, 1938; Hue et al., 2006; Lima and Magalhães, 2018).

Another relevant drought according to TRA5 is centered around 1620 CE (point 3 of Fig. 6). This drought is recorded in historical documents and lasted from 1614 to 1615 CE, although it did not have the same socioeconomic impact as the two prior droughts (Lima and Magalhães, 2018). In fact, between the 16th and 17th century there are few historical drought records (period A in Fig 6). One hypothesis to explain this hiatus is the low population density of the NEB territory, resulting in poor historical documentation of such events. However, according to the TRA5 record, between the event 2 ~1564 CE and event 4 ~1717 CE (Fig. 6), the only drought peak occurs in 1620 CE, confirming an almost

688   150-year long period of relative climate stability with prevailing wet conditions in NEB.

689   These favorable conditions certainly helped with the initial population establishment at the

690   beginning of 16th century, and led to the peak era of sugar cane production in NEB around

691   1650 CE along coastal areas (Taylor, 1970).

692   During the 18th century NEB experienced a significant increase in rural population,

693   characterized by the establishment of large cattle farms (Fausto, 2006). In this period,

694   three droughts are documented in the TRA5 record (Fig. 6). The $\delta^{18}O$ excursion around

695   1717 CE (point 4 in Fig. 6) can be associated with the drought that lasted from 1720 to

696   1727 CE; the first big drought in NEB, which according to historical documents, caused the

697   mortality of wildlife and cattle, and affected the agricultural productivity. Entire Indigenous

698   tribes died of starvation as a consequence of this drought and a concurrent smallpox

699   (variola) epidemic, which also killed other ethnic groups, especially the native population

700   and black people enslaved during that period (Alves, 1929).

701   The following event around 1740 CE (point 5 in Fig. 6) was also recorded in

702   historical documents, but did not seem to be associated with major impacts. However, all

703   of these droughts were probably responsible for a drop in sugar-cane exports to Europe

704   during the first half of the 18th century (Galloway, 1975).

705   Another drought occurred from 1776 to 1778 CE, and is imprinted in our record

706   around 1770 CE (point 6 in Fig. 6). This event was again accompanied by a variola

707   outbreak probably spread by a lowering in the sanitary conditions and increased people

708   agglomeration. The association between this disease and droughts might explain the

709   economic and health crisis, since people started to migrate to the cities looking for

710   treatment and food, leading the Brazilian Governor to transfer infected people to isolated

711   lands, resulting in thousands of deaths (Rosado, 1981). Finally, the most recent peak in

712   our data displays an event around 1835 CE (point 7 of Fig. 6), associated with a drought

713   that lasted from 1833 to 1835 CE, reaching the northernmost areas of NEB, and leading to

714   the largest human migration to other Brazilian regions (Lima and Magalhães, 2018). The

715   droughts centered around 1770 and 1835 CE had a huge impact on society according the

716   historical records (Lima and Magalhães, 2018).

717   Although the precision of the TRA5 speleothem chronology is reduced during the

718   last ~150 years, we observe that the wet period from the 1940s to the 1970s (line B in Fig.

719   6) is coincident with the mid-20th century break in global warming that has been discussed

720   as being forced by aerosol emissions (e.g., Booth et al., 2012; Undorf et al., 2018). Our

721   data suggest an increased precipitation in this period that is supported by a trend in

722   decreasing values of $\delta^{18}O$ in corals from the northeast coast of N-NEB, equally interpreted

723   as an ITCZ southward displacement caused by a decreasing SST gradient between the

724   North and South Atlantic (Pereira et al., 2022).

725   Our TRA5 stalagmite data record some of the most important droughts that

726   occurred in NEB between the 16th and the 18th centuries, demonstrating the potential of

727   stalagmite studies in monitoring abrupt and extreme climate events through time.

728   However, the speleothems do not record all documented historical dry events, as some

729   droughts may not have affected the Trapiá Cave region, or they were not strong or long

730   enough to affect the isotopic signal of the groundwater storage in the epikarst.

731   Furthermore, the period between 1620 and 1717 CE is devoid of any abrupt drought

732   events in the TRA5 stalagmite, which is again consistent with the historical records. It is

733   also important to mention that Lima and Magalhães (2018) report all drought events in

734   NEB and do not indicate their location. We suggest that progressive changes in the mean

735   ITCZ position along the last 500 years might be responsible for historical droughts that

736   affected the seasonality of N-NEB and caused abrupt and strong drought events.

737   Additional drought-sensitive high-resolution records will be required to improve our

738   understanding of these historical droughts events in NEB.

739

6. Conclusions

We present the first high-resolution record for the ITCZ in N-NEB that covers the last 3200 years and also records the major historical droughts that took place in NEB during the last 500 years. Based on stalagmite oxygen isotopes, we describe the regions' paleoclimate variability for the last 2500 years and its connections to remote forcing mechanisms such as the AMV and changes in Pacific and Atlantic SST gradients.

The N-NEB record presents a trend toward drier conditions from 1000 BCE to 1500 CE as is also being observed in the Diva de Maura Cave in S-NEB, interpreted as an ITCZ contraction and SASM weakening on an orbital timescale, respectively. Although the two records are influenced by distinctly different climate systems with different precipitation seasonality, ITCZ and SASM dynamics are known to be closely linked (Vuille et al., 2012).

During the last millennia, ITCZ dynamics in the tropical Atlantic – South America sector cannot be explained solely by north-south ITCZ migrations or one single forcing mechanism. We propose a zonally non-uniform behavior of the ITCZ during the event centered around 1100 CE and the drought events between 1500 and 1750 CE, when the RN record is anti-phased with the Paraíso cave record from the eastern Amazon. This zonal behavior would be forced by the interactions between AMV and PDV modes that changed the regional Walker cell position and ITCZ intensity/extent and thus affecting precipitation variability between the eastern Amazon and N-NEB.

The historical droughts discussed are the longest drought events in Northeast Brazil that occurred within the zone of influence of the ITCZ, and are thus probably the most likely to be recorded by stalagmites, according to our interpretation. The northern and southern NEB are influenced by different climatic systems, the ITCZ and SASM, respectively, and this can explain, in part, the differences between historical and stalagmite records of Rio Grande do Norte. These historical droughts recorded in the RN stalagmite suggest that much of the socioeconomic development of the NEB, which

766   occurred after 1500 CE, benefitted from conditions that were unusually humid in a long-

767   term context. During the last 500 years the technological development, infrastructure,

768   civilization and population growth relied on more abundant resources. On the other hand,

769   our data also shows how short, abrupt drought events significantly affected human

770   population and other life forms, especially when associated with anthropogenic changes in

771   the environment. These droughts induced an environment favorable for spreading of

772   disease, starvation, lack of water, environmental degradation and crowding of people

773   seeking help, among other problems. These events demonstrate the social and

774   environmental impacts associated with extreme events in this vulnerable environment and

775   our speleothem work documents the enormous potential of these archives to reconstruct

776   the drought history in this region.

777

796

Data availability

798 The dataset generated as part of this study will be available in the PANGAEA

799 website.

800

Author contribution

802 G.U. and F.W.C designed the experiment, performed isotopic analysis and

803 prepared the manuscript with help from the coauthors; F.W.C. directed the project and

804 revised all versions of manuscript; M.V. helped with the interpretation and revision of the

805 manuscript; A.A. contributed with statistical analysis and interpretation; V.F.N. contributed

806 with the paleoclimate interpretations and revision of the manuscript; G.S. and J.M. helped

807 with interpretation and revision of the manuscript; F.R.D.A. provided and interpreted the

808 mineralogical analysis; H.Z. helped with U/Th analysis and revision of the manuscript, and

809 H.C. and R.L.E. coordinated the laboratory procedures for U/Th analysis.

810

Competing interests

812 The authors declare that they have no known competing financial interests or

813 personal relationships that could have appeared to influence the work reported in this

814 paper.

815

References

Alvalá, R.C.S., Cunha, A.P.M.A., Briton, S.S.B., Seluchi, M.E., Marengo, J.A., Moraes, O.L.L., Carvalho, M.A.: Drought monitoring in the Brazilian Semiarid region, An. Acad. Bras. Ciênc., 91 (1), e20170209, https://doi.org/10.1590/0001-3765201720170209, 2019.

Alves, J.: História das secas (século XVII a XIX). Fundação Waldemar Alcântara, Fortaleza, https://colecaomossoroense.org.br/site/wp-content/uploads/2018/07/HISTÓRIA-DAS-SECAS.pdf, last accessed: 21 16 March August 2023. 2003.

ANA – Agência Nacional de Águas, Sistema Nacional de Informações sobre Recursos Hídricos: http://www.snirh.gov.br/hidroweb/apresentacao, last accessed: 01 February 2022, 2013.

Andreoli, R. F. S., de Souza, R.A.F., Kayano, M.T., Candido, L.A.: Seasonal anomalous rainfall in the central and eastern Amazon and associated anomalous oceanic and atmospheric patterns, Int. J. Climatol., 32, 1193–1205, https://doi.org/10.1002/joc.2345, 2011.

Apaéstegui, J., Cruz, F.W., Vuille, M., Fohlmeister, J., Espinoza, J.C., Sifeddine, A., Strikis, N., Guyot, J.L., Ventura, R., Cheng, H., Edwards, R.E.: Precipitation changes over the eastern Bolivian Andes inferred from speleothem (δ^{18}O) records for the last 1400 years, Earth Planet. Sci. Lett., 494, 124–134, https://doi.org/10.1016/j.epsl.2018.04.048, 2018.

Araújo, R.G., Andreoli, R.V., Candido, L.A., Kayano, M.T., de Souza, R.A.F.: Influence of El Niño-Southern Oscillation and Equatorial Atlantic on rainfall over northern and northeastern regions of South America, Acta Amaz., 43, 4, 469-480, https://doi.org/10.1590/S0044-59672013000400009, 2013.

Azevedo, V., Strikis, N.M., Novello, V.F., Roland, C.L., Cruz, F.W., Santos, R.V., Vuille, M., Utida, G., de Andrade, F.D., Cheng, H., Edwards, R.L.: Paleovegetation seesaw in

843   Brazil since the Late Pleistocene: A multiproxy study of two biomes, Earth Planet. Sci.

844   Lett., 563, 116880, https://doi.org/10.1016/j.epsl.2021.116880, 2021.

845 Baker, A., Hartmann, A., Duan, W., Hankin, S., Comas-Bru, L., Cuthbert, M.O., Treble,

846   P.C., Banner, J., Genty, D., Baldini, L.M., Bartolomé, M., Moreno, A., Pérez-Mejías, C.,

847   Werner, M.: Global analysis reveals climatic controls on the oxygen isotope

848   composition of cave drip water. Nat. Commun., 10, 2984.

849   https://doi.org/10.1038/s41467-019-11027-w, 2019.

850 Bond, G., Kromer, B., Beer, Muscheler, R., Evans, M.N., Showers, W., Hoffmann, S., Lotti-

851   Bond, R., Hajdas, I., Bonani, G.: Persistent Solar Influence on North Atlantic Climate

852   During the Holocene, Science, 294, 2130-2136,

853   https://doi.org/10.1126/science.1065680, 2001.

854 Booth, B.B.B., Dunstone, N.J., Halloran, et al., P.R., Andrews, T., Bellouin, N.: Aerosols

855   implicated as a prime driver of twentieth-century North Atlantic climate variability,

856   Nature, 484, 228-232, https://doi.org/10.1038/nature10946, 2012.

857 Breitenbach, S.F.M., Rehfeld, K., Goswami, B., Baldini, J.U.L., Ridley, H. E., Kennett, D.

858   J., Prufer, K.M., Aquino, V.V., Asmerom, Y., Polyak, V.J., Cheng, H., Kurths, J.,

859   Marwan, N.: COnstructing Proxy Records from Age models (COPRA), Clim. Past, 8,

860   1765–1779, https://doi.org/10.5194/cp-8-1765-2012, 2012.

861 Broccoli, A. J., Dahl, K.A., Stouffer, R.J.: Response of the ITCZ to Northern Hemisphere

862   cooling, Geophys. Res. Lett., 33, L01702, https://doi.org/10.1029/2005GL024546,

863   2006.

864 Campos, J.L.P.S., Cruz, F.W., Ambrizzi, T., Deininger, M., Vuille, M., Novello, V.F., Strikis,

865   N.M.: Coherent South American Monsoon Variability During the Last Millennium

866   Revealed Through High-Resolution Proxy Records, Geophys. Res. Lett., 46, 8261–

867   8270, https://doi.org/10.1029/2019GL082513, 2019.

868 Campos, M.C.; Chiessi, C.M.; Novello, V.F.; Crivellari, S.; Campos, J.L.P.S.; Albuquerque,

869   A.L.S.; Venancio, I.M.; Santos, T.P.; Melo, D.B.; Cruz, F.W.; Sawakuchi, A.O.;

870   Mendes, V.R.: South American precipitation dipole forced by interhemispheric

871   temperature gradient, Sci. Rep., 12, 10527, https://doi.org/10.1038/s41598-022-14495-

872   1, 2022.

873 Cheng, H., Edwards, R.L., Shen, C-C., Polyak, V.J., Asmerom, Y., Woodhead, J.,

874   Hellstrome, J., Wang, Y., Kong, X., Spötlg, C., Wang, X., Alexander Jr. E.C.:

875   Improvements in ^{230}Th dating, ^{230}Th and ^{234}U half-life values and U-Th isotopic

876   measurements by multi-collector inductively coupled plasma mass spectrometry, Earth

877   Planet. Sci. Lett., 371-372, 82-91, https://doi.org/10.1016/j.epsl.2013.04.006, 2013.

878 Chiessi, C. M., Mulitza, S., Taniguchi, N.K., Prange, M., Campos, M.C., Häggi, C.,

879   Schefuß, E., Pinho., T.M.L., Frederichs, T., Portilh-Ramos, R.C., Souza, S.H.M.,

880   Crivellari, S., Cruz, F.W.: Mid- to late-Holocene contraction of the Intertropical

881   Convergence Zone over northeastern South America, Paleocean. Paleoclim., 36,

882   e2020PA003936, https://doi.org/10.1029/2020PA003936, 2021.

883 Cruz, F.W., Vuille, M., Burns, S.J., Wang. X., Cheng, H., Werner, M., Edwards, R.L.,

884   Karman, I., Auler, A.S., Nguyen, H.: Orbitally driven east-west antiphasing of South

885   American precipitation, Nat. Geosci., 2, 210-214, https://doi.org/10.1038/ngeo444,

886   2009.

887 Dansgaard, W.: Stable isotopes in precipitation, Tellus XVI, 4, 436-468,

888   https://doi.org/10.1111/j.2153-3490.1964.tb00181.x, 1964.

889 De Oliveira, P.E., Barreto, A.M.F., Suguio, K.: Late Pleistocene-Holocene climatic and

890   vegetational history of the Brazilian Caatinga: the fossil dunes of the middle São

891   Francisco River, Palaeogeogr. Palaeoclimatol. Palaeoecol., 152, 319-337,

892   https://doi.org/10.1016/S0031-0182(99)00061-9, 1999.

893 Della Libera, M.E., Novello, V.F., Cruz, F.W., Orrison, R., Vuille, M., Maezumi, S.Y., de

894   Souza, J., Cauhy, J., Campos, J.L.P.S., Ampuero, A., Utida., G., Stríkis, N.M., Stumpf,

895   C.F., Azevedo, V., Zhang, H., Edwards, R.L., Cheng. H.: Paleoclimatic and

896   paleoenvironmental changes in Amazonian lowlands over the last three millennia,

897   Quat. Sci. Rev., 279, 107383, https://doi.org/10.1016/j.quascirev.2022.107383, 2022.

898 Edwards, R. L., Cheng, H., Wasserburg, J.: ^{238}U- ^{234}U-^{230}Th- ^{232}Th systematics and the

899   precise measurement of time over the past 500,000 years. Earth Planet. Sci. Lett*., 81,

900   175-92, https://doi.org/10.1016/0012-821X(87)90154-3, 1987.

901 Erasmi, S., Maurer, F., Petta, R.A., Gerold, G., Barbosa, M.P.: Interannual variability of the

902   Normalized Difference Vegetation Index over Northeast Brazil and its relation to rainfall

903   and El Niño Southern Oscillation, Geo-Öko, 30, 3-4, 185-206, 2009.

904 Fausto, B.: História do Brasil, 12th ed., Editora Universidade de São Paulo, São Paulo,

905   660 pp., ISBN 85-314-0240-9, 2006.

906 Fohlmeister, J.: A statistical approach to construct composite climate records of dated

907   archives, Quat. Geochronol., 14, 48-56, https://doi.org/10.1016/j.quageo.2012.06.007,

908   2012.

909 Galloway, J.H.: Northeast Brazil 1700-50: The agricultural crisis re-examined, J. Hist.

910   Geogr., 1, 1, 21-38, https://doi.org/10.1016/0305-7488(75)90073-0, 1975.

911 Gomes, H.B., Ambrizzi, T., Herdies, D.L., Hodges, K., da Silva, B.F.P.: Easterly Wave

912   Disturbances over Northeast Brazil: An Observational Analysis, Adv. Meteorol.,

913   176238, https://doi.org/10.1155/2015/176238, 2015.

914 Grazulis, S., Chateigner, D., Downs, R.T., Yokochi, A.F.T., Quirós, M., Lutterotti, L.,

915   Manakova, E., Butkus, J., Moeck., P., Le Bail., A.: Crystallography Open Database –

916   an open-access collection of crystal structures, J. Appl. Crystallogr., 42, 726-729,

917   https://doi.org/10.1107/S0021889809016690, 2009.

Haug, G., Hughen, K.A., Sigman, D.M., Peterson, L.C., Röhl, U.: Southward migration of the Intertropical Convergence Zone through the Holocene, Science, 293, 5533, 1304-1308, https://doi.org/10.1126/science.1059725, 2001.

He, Z., Dai, A., Vuille, M.: The Joint Impacts of Atlantic and Pacific Multidecadal Variability on South American Precipitation and Temperature, J. Clim., 34, 7959-7981, https://doi.org/10.1175/JCLI-D-21-0081.1, 2021.

Hue, S. M.: Primeiras Cartas do Brasil 1551-1555: Introdução e notas, Jorge Zahar Editor, Rio de Janeiro, 147 pp., ISBN 8571109079, 2006.

IAEA/GNIP - Global Network of Isotopes in Precipitation, The GNIP Database, https://nucleus.iaea.org/wiser, last access: 20 August 2021.

INMET - Instituto Nacional de Meteorologia, Banco de Dados Meteorológicos para Ensino e Pesquisa, http://www.inmet.gov.br/, last access 5 November 2021.

Jackson, L.C., Kahana, R., Graham, T., Ringer, M.A., Woollings, T., Mecking, J.V., Wood, R.A.: Global and European climate impacts of a slowdown of the AMOC in a high resolution GCM, Clim. Dyn., 45, 3299–3316, https://doi.org/10.1007/s00382-015-2540-2, 2015.

Jaffey, A.H., Flynn, K.F., Glendenin, L.E., Bentley, W.C., Essling, A.M., Precision measurement of half-lives and specific activities of ^{235}U and ^{238}U. Physical Rev. C 4, 1889-1906, https://doi.org/10.1103/PhysRevC.4.1889, 1971.

Kayano, M.T., Andreoli, R.V., de Souza, R.A.: Pacific and Atlantic multidecadal variability relations to the El Niño events and their effects on the South American rainfall, Int. J. Clim., 40(4), 2183-2200, https://doi.org/10.1002/joc.6326, 2020.

Kayano, M.T., Cerón, W.L., Andreoli, R.V., Souza, R.A.F., Avila-Diaz, A., Zuluaga, C.F., Carvalho, L.M.V.: Does the El Niño-Southern Oscillation Affect the Combined Impact of the Atlantic Multidecadal Oscillation and Pacific Decadal Oscillation on the

943   Precipitation and Surface Air Temperature Variability over South America?, Atmos., 13,

944   231, https://doi.org/10.3390/atmos13020231, 2022.

945 Knight, J.R., Folland, C.K., Scaife, A.A.: Climate impacts of the Atlantic Multidecadal

946   Oscillation, Geophys. Res. Let., 33, L17706, https://doi.org/10.1029/2006GL026242,

947   2006.

948 Lachniet, M.S., Bernal, J.P., Asmerom, Y., Polyak, V., Uranium loss and aragonite–calcite

949   age discordance in a calcitized aragonite stalagmite, Quat. Geochron., 14, 26-37,

950   https://doi.org/10.1016/j.quageo.2012.08.003, 2012.

951 Lapointe, F., Bradley, R.S., Francus, P., Balascio, N.L., Abbott, M.B., Stoner, J.S., St-

952   Onge, G., De Coninck, A., Labarre, T.: Annually resolved Atlantic Sea surface

953   temperature variability over the past 2,900 y, PNAS, 117, 44, 27171–27178,

954   https://doi.org/10.1073/pnas.2014166117, 2020.

955 Lechleitner, F. A., Breitenbach, S.F.M., Rehfeld, K., Ridley, H.E., Asmerom, Y., Prufer,

956   K.M., Marwan, N., Goswami, B., Kennett, D.J., Aquino, V.V., Polyak, V., Haug, G.H.,

957   Eglinton, T.I., Baldini, J.U.L.: Tropical rainfall over the last two millennia: Evidence for a

958   low-latitude hydrologic seesaw, Sci. Rep., 7, 45809, https://doi.org/10.1038/srep45809,

959   2017.

960 Lenters, J. D., Cook, K. H.: On the origin of the Bolivian High and related circulation

961   features of the South American climate, J. Atmos. Sci., 54, 656–677,

962   https://doi.org/10.1175/1520-0469(1997)054<0656:OTOOTB>2.0.CO;2, 1977.

963 Levine, A.F.Z., Frierson, D.M.W., McPhaden, M.J.: AMO Forcing of Multidecadal Pacific

964   ITCZ Variability, J. Clim., 31, 5749–5764, https://doi.org/10.1175/JCLI-D-17-0810.1,

965   2018.

966 Lima, J.R., Magalhães, A.R.: Secas no Nordeste: registros históricos das catástrofes

967   econômicas e humanas do século 16 ao século 21, Parcer. Estratég., 23, 46, 191-212,

968   2018. Available at: https://seer.cgee.org.br/parcerias_estrategicas/article/view/896/814.

969   Maksic J., Shimizu, M.H., Kayano, M.T., Chiessi, C.M., Prange, M., Sampaio, G.: Influence

970   of the Atlantic Multidecadal Oscillation on South American Atmosphere Dynamics and

971   Precipitation, Atmos., 13, 11, 1778, https://doi.org/10.3390/atmos13111778, 2022.

972   Marengo, J.A., Bernasconi, M.: Regional differences in aridity/drought conditions over

973   Northeast Brazil: present state and future projections, Clim. Chang., 129, 103-115,

974   https://doi.org/10.1007/s10584-014-1310-1, 2015.

975   McDonough, W.F., Sun, S.-s.: The composition of the Earth, Chem. Geol., 120, (3–4) 223-

976   253, ISSN 0009-2541, https://doi.org/10.1016/0009-2541(94)00140-4, 1995.

977   Melo, A.C.C., Castro, D.L., Bezerra, F.H.R., Bertotti, G.: Rift fault geometry and evolution

978   in the Cretaceous Potiguar Basin (NE Brazil) based on fault growth models, J. South

979   Am. Earth Sci., 71, 96-107, https://doi.org/10.1016/j.jsames.2016.07.006, 2016.

980   Novello, V.F., Cruz, F.W., Karmann, I., Burns, S.J., Stríkis, N.M., Vuille, M., Cheng, H.,

981   Edwards, R.L., Santos, R.V., Frigo, E., Barreto, E.A.S.: Multidecadal climate variability

982   in Brazil's Nordeste during the last 3000 years based on speleothem isotope records,

983   Geophys. Res. Lett., 39, L23706, https://doi.org/10.1029/2012GL053936, 2012.

984   Novello, V.F., Cruz, F.W., Moquet, J.S., Vuille, M., de Paula, M.S., Nunes, D., Edwards,

985   R.L., Cheng, H., Karmann, I., Utida, U., Stríkis, N.M., Campos, J.L.P.S.: Two Millennia

986   of South Atlantic Convergence Zone Variability Reconstructed from Isotopic Proxies,

987   Geophys. Res. Lett., 45, https://doi.org/10.1029/2017GL076838, 2018.

988   Novello, V.F., Cruz, F.W., Vuille, M., Campos, J.L.P.S., Stríkis, N.M., Apaéstegui, J.,

989   Moquet, J.S., Azevedo, V., Ampuero, A., Utida, G., Wang, X., Paula-Santos, G.M.,

990   Jaqueto, P., Pessenda, L.C.R., Breecker, D.O., Karmann, I.: Investigating δ^{13}C values

991   in stalagmites from tropical South America for the last two millennia, Quat. Sci. Rev.,

992   255, 106822, https://doi.org/10.1016/j.quascirev.2021.106822, 2021.

993   Orrison, R., Vuille, M., Smerdon, J.E., Apaéstegui, J., Azevedo, V., Campos, J.L.P.S.,

994   Cruz, F.W., Della Libera, M.E., Stríkis, N.M.: South American Monsoon variability over

995   the last millennium in paleoclimate records and isotope-enabled climate models, Clim.

996   Past, 18, 2045–2062, https://doi.org/10.5194/cp-18-2045-2022, 2022.

997   Paquette, J., Reeder, R.J.: Single-crystal X-ray structure refinements of two biogenetic

998   magnesian calcite crystals, Am. Mineral., 75, 1151-1158, 1990.

999   Pereira, N.S., Clarke, L.J., Chiessi, C.M., Kilbourne, K.H., Crivellari, S., Cruz, F.W.,

1000   Campos, J.L.P.S., Yu, T.-L., Shen, C.-C., Kikuchi, R.K.P., Pinheiro, B.R., Longo, G.O.,

1001   Sial, A.N., Felis, T.: Mid to late 20th century freshening of the western tropical South

1002   Atlantic triggered by southward migration of the Intertropical Convergence Zone,

1003   Palaeogeogr.   Palaeoclimatol.   Palaeoecol.,   597,   111013,

1004   https://doi.org/10.1016/j.palaeo.2022.111013, 2022.

1005   Pessenda, L.C.R., Gouveia, S.E.M., Ribeiro, A.S., De Oliveira, P.E., Aravena, R.: Late

1006   Pleistocene and Holocene vegetation changes in northeastern Brazil determined from

1007   carbon isotopes and charcoal records in soils, Palaeogeogr. Palaeoclimatol.

1008   Palaeoecol., 297, 597-608, https://doi.org/10.1016/j.palaeo.2010.09.008, 2010.

1009   Pessoa-Neto, O.C.: Estratigrafia de sequências da plataforma mista neogênica na Bacia

1010   Potiguar, margem equatorial brasileira, Revista Bras. Geociênc., 33, 3, 263-278, 2003.

1011   Pokroy, B., Fieramosca, J. S., Von Dreele, R. B., Fitch, A. N., Caspi, E. N., Zolotoyabko,

1012   E.: Atomic structure of biogenic aragonite, Chem. Mater., 19, 3244-3251,

1013   https://doi.org/10.1021/cm070187u, 1989.

1014   Richards, D., Dorale, J.: Uranium-series chronology and environmental applications of

1015   speleothems. Rev. Mineral., 52, 407-460, https://doi.org/10.2113/0520407, 2003.

1016   Rosado, J. V.-U. (org): Memorial da Seca. Brasília, Coleção Mossoroense, nº 163, Centro

1017   Gráfico do Senado Federal/ESAM, https://colecaomossoroense.org.br/site/acervo-

1018   oswaldo-lamartine/, last access: 25 August 2022, 1981.

1019   Sampaio, P.R.F., Saraiva Jr, J.C., Portela, J.C., da Silva, J.F.: Agricultural areas to

1020   desertification in RN and mitigating measures: the case of settlements Milagres and

1021   Terra da Esperança, HOLOS, 36, 7, e5902, https://doi.org/10.15628/holos.2020.5902,

1022   2020.

1023   Schneider, T., Bischoff, T., Haug, G.H.: Migrations and dynamics of the intertropical

1024   convergence zone, Nature, 513, 7516, 45-53, https://doi.org/10.1038/nature13636,

1025   2014.

1026   Schneider, U., Becker, A., Finger, P., Meyer-Christoffer, A., Rudolf, B., Ziese, M.: GPCC

1027   Full Data Reanalysis Version 6.0 at 1.0°: Monthly Land-Surface Precipitation from

1028   Rain-Gauges   built   on   GTS-based   and   Historic   Data,

1029   https://doi.org/10.5676/DWD_GPCC/FD_M_V7_100, 2011.

1030   Serafim Leite, S.J.: História da Companhia de Jesus no Brasil, Tomo II (Século XVI - A

1031   Obra), Civilização Brasileira, Rio de Janeiro, 658 pp. 1938.

1032   Silva, O.L., Bezerra, F.H.R., Maia, R.P., Cazarin, C.L.: Karst landforms revealed at various

1033   scales using LiDAR and UAV in semi-arid Brazil: Consideration on karstification

1034   processes   and   methodological   constraints,   Geomorphol.,   295,   611-630,

1035   https://doi.org/10.1016/j.geomorph.2017.07.025, 2017.

1036   Steinman, B.A., Stansell, N.D., Mann, M.E., Cooke, C.A., Abbott, M.B., Vuille, M., Bird,

1037   B.W., Lachniet, M.S., Fernandez, A.: Interhemispheric antiphasing of neotropical

1038   precipitation   during   the   past   millennium,   PNAS,   119,   17,   e2120015119,

1039   https://doi.org/10.1073/pnas.2120015119, 2022.

1040   Sulca, J., Vuille, M., Silva, Y., Takahashi, K.: Teleconnections between the Peruvian

1041   Central Andes and Northeast Brazil during Extreme Rainfall Events in Austral Summer,

1042   J. Hydrometeorol., 17, 499-515, https://doi.org/10.1175/JHM-D-15-0034.1, 2016.

1043   Taylor, K.S.: The Economics of Sugar and Slavery in Northeastern Brazil, Agric. Hist., 44

1044   3, 267-280, 1970.

1045   Treble, P.C., Baker, A., Abram, N.J., Hellstrom, J.C., Crawford, J., Gagan, M.K., Borsato,

1046   A., Griffiths, A.D., Bajo, P., Markowska, M., Priestley, S.C., Hankin, S., Paterson, D.:

Ubiquitous karst hydrological control on speleothem oxygen isotope variability in a global study, Commun. Earth Environ., 3, 29, https://doi.org/10.1038/s43247-022-00347-3, 2022.

Undorf, S., Bollasina, M.A., Hegerl, G.C.: Impacts of the 1900–74 Increase in Anthropogenic Aerosol Emissions from North America and Europe on Eurasian Summer Climate, J. Clim., 31, 8381-8399, https://doi.org/10.1175/JCLI-D-17-0850.1, 2018.

Utida, G., Cruz, F.W., Etourneau, J., Bouloubassi, I., Schefuß, E., Vuille, M., Novello, V., Prado, L.F., Sifeddine, A., Klein, V., Zular, A., Viana, J.C.C., Turcq, B.: Tropical South Atlantic influence on Northeastern Brazil precipitation and ITCZ displacement during the past 2300 years, Sci. Rep., 9, 1698, https://doi.org/10.1038/s41598-018-38003-6, 2019.

Utida, G., Cruz, F.W., Santos., R.V., Sawakuchi, A.O., Wang, H., Pessenda, L.C.R., Novello, V.F., Vuille, M., Strauss, A.M., Borella, A.C., Stríkis, N.M., Guedes, C.C.F., De Andrade, F.D., Zhang., H., Cheng, H., Edwards, R.L.: Climate changes in Northeastern Brazil from deglacial to Meghalayan periods and related environmental impacts, Quat. Sci. Rev., 250, 106655, https://doi.org/10.1016/j.quascirev.2020.106655, 2020.

Vera, C., Higgins, W., Amador, J., Ambrizzi, T., Garreaud, R., Gochis, D., Gutzler, D., Lettenmaier, D., Marengo, J., Mechoso, C.R., Nogues-Paegle, J., Silva Dias, P.L., Zhang, C.: Toward a Unified View of the American Monsoon Systems, J. Clim., 19, 4977-5000, https://doi.org/10.1175/JCLI3896.1, 2006.

Vuille, M., Burns, S.J., Taylor, B.L., Cruz, F.W., Bird, B.W., Abbott, M.B., Kanner, L.C., Cheng, H., Novello, V.F.: A review of the South American monsoon history as recorded in stable isotopic proxies over the past two millennia, Clim. Past, 8, 1309–1321, https://doi.org/10.5194/cp-8-1309-2012, 2012.

1072 Wang, X., Edwards, R.L., Auler, A.S., Cheng, H., Kong, X., Wnag, Y., Cruz, F.W., Dorale,

1073   J.A., Chiang, H.-W.: Hydroclimate changes across the Amazon lowlands over the past

1074   45,000 years, Nature, 541, 204-207, https://doi.org/10.1038/nature20787, 2017.

1075 Wong, M.L.; Wang, X.; Latrubesse, E.M.; He, S.; Bayer, M.: Variations in the South

1076   Atlantic Convergence Zone over the mid-to-late Holocene inferred from speleothem

1077 δ^{18}O in central Brazil, Quat. Scie. Rev., 270, 107178,

1078   https://doi.org/10.1016/j.quascirev.2021.107178, 2021.

1079 Zhang, H., Cai, Y., Tan, L., Cheng, H., Qin, S., An, Z., Edwards, R.L., Ma, L.: Large

1080   variations of δ^{13}C values in stalagmites from southeastern China during historical

1081   times: implications for anthropogenic deforestation, Boreas, 44, 511-525,

1082   https://doi.org/10.1111/bor.12112, 2015.

1083 Zhang, H., Cai, Y., Tan, L., Qin, S., An, Z.: Stable isotope composition alteration produced

1084   by the aragonite-to-calcite transformation in speleothems and implications for

1085   paleoclimate reconstructions, Sediment. Geol., 309, 1-14,

1086   https://doi.org/10.1016/j.sedgeo.2014.05.007, 2014.

1087 Ziese, M., Rauthe-Schöch, A., Becker, A., Finger, P., Meyer-Christoffer, A., Schneider, U.:

1088   GPCC Full Data Daily Version 2018 at 1.0°: Daily Land-Surface Precipitation from

1089   Rain-Gauges built on GTS-based and Historic Data [datset],

1090   https://doi.org/10.5676/DWD_GPCC/FD_D_V2018_100, 2018.

1091 Zilli, M.T.; Carvalho, L.M.V.; Lintnerm, B.R., The poleward shift of South Atlantic

1092   Convergence Zone in recent decades, Clim. Dyn., 52, 2545-2563,

1093   https://doi.org/10.1007/s00382-018-4277-1, 2019.

1094 Zular, A., Utida, G., Cruz, F.W., Sawakuchi, A.O., Wang, H., Bícego, M. Giannini, P.C.F.,

1095   Rodrigues, S.I., Garcia, G.P.B., Vuille, M., Sifeddine, A., Zocatelli. R., Turcq, B.,

1096   Mendes, V.R.: The effects of mid-Holocene fluvio-eolian interplay and coastal

1097   dynamics on the formation of dune-dammed lakes in NE Brazil, Quat. Sci. Rev., 196,

1098   137–153, https://doi.org/10.1016/j.quascirev.2018.07.022, 2018.